Polarimetric Behavior for the Derivation of Sea Ice Topographic Height From TanDEM-X Interferometric SAR Data

Lanqing Huang , *Student Member, IEEE*, and Irena Hajnsek , *Fellow, IEEE*

Abstract—Single-pass interferometric synthetic aperture radar (InSAR) is an effective technique for sea ice topographic retrieval despite the inherent dynamics of sea ice. However, the penetration of microwaves into snow-covered thick ice and the achievable height sensitivity for tens-of-centimeters thin ice are two major issues, which limit the accuracy of InSAR-derived sea ice topography. Polarimetry provides scattering information concerning the sea ice properties and has the potential, in combination with interferometry, to achieve an accurate reconstruction of a sea ice digital elevation model (DEM). This article studies the relation between polarimetric signatures and sea ice topography, and explores the possibility to compensate the penetration bias by merging copolar coherence into InSAR processing. The newly generated topographic map has a root-mean-square error under 0.3 m. For thin ice below 1 m, a positive relation between copolar phase ϕ_{coPol} and surface height is observed, suggesting that ϕ_{coPol} can effectively characterize thin sea ice topography. For thick ice with ridges, the maximum polarimetric phase difference $\Delta\phi_{\mathrm{maxPol}}$ reveals a particular shape of the coherence region, which can be interpreted as oriented volume scattering. It suggests that the model-based approach using polarimetric SAR interferometry assuming an oriented volume scattering model is promising in measuring the scattering centers in thick and deformed sea ice. The study of polarimetric behavior for the InSAR DEM is, therefore, a step forward toward accurate modeling of sea ice topography from polarimetric single-pass InSAR data.

Index Terms—Polarimetry, sea ice topography, single-pass interferometry, TanDEM-X.

I. INTRODUCTION

SEA ice is frozen ocean water floating on the ocean surface found in remote polar oceans. The forces from wind and ocean currents combined with the blocking effects at the coast and islands act on ice, resulting in an irregular spatial change of ice features. The macroscale sea ice topography is complicated due to different ice features such as rafted ice, pressure ridges, and hummocks [1], [2]. The snow pack on top of the sea ice is also influencing the ice surface and, thus, further complicate the sea ice topography [3].

The knowledge of sea ice topography on spatial scales of meters is valuable for understanding the processes occurring between the ice and the atmosphere boundary [4], [5]. Variation of surface topography affects turbulent transfers of heat and momentum [6], acting as an important variable in the atmosphere-ice-ocean system. Besides, characterization of sea ice topography is relevant to assess the effects of environmental impacts on animals and their habitats [7], [8]. The relations between Antarctic sea ice biological communities and sea ice morphological processes (e.g., flooded snow layer and pressure ridge) are summarized in [9]. Furthermore, topographic information of landfast ice is crucial to the trafficability assessment [10] for local communities and industry. A trafficability index was derived from ridge topography and surface roughness to guide routes for various modes of transportation [11]. As a result, precise characterization of the sea ice topography for various ice types has been a topic of active research for decades.

The sea ice topography has been measured by several instruments, including stereo camera data using photogrammetric techniques [12], [13] and laser altimeters equipped on various platforms (e.g., helicopter [14], aircraft [15], and satellite [16], [17]). The Ice, Cloud, and land Elevation Satellite (ICESat) [16] and its follow-on mission ICESat-2 [17], are the benchmark spaceborne laser altimeter missions for measuring the topography of ice sheets and sea ice over Antarctica and Greenland. However, the major limitation of the measurements above is small spatial coverage. Synthetic aperture radar (SAR) has become an invaluable asset for monitoring polar regions since it is capable of providing continuous all-weather day/night imagery with wide spatial coverage. Interferometric SAR (InSAR) offers an opportunity to estimate surface height from two or more image pairs [18]. However, it is impossible to estimate the height over sea ice from one SAR instrument which needs tens of hours to several days to acquire the image pairs. Due to the dynamic nature of sea ice, such temporal gap would lead to a large interferometric decorrelation between the image pairs and impede the accuracy of height retrieval. The estimation of sea ice topographic height was becoming possible with the radar mission TanDEM-X [19]. TanDEM-X is a single-pass

Lanqing Huang is with the Institute of Electronic Engineering, Shanghai Jiao Tong University, Shanghai 200240, China, and also with the Institute of Environmental Engineering, Swiss Federal Institute of Technology, 8093 Zürich, Switzerland (e-mail: lanqing.huang93@gmail.com).

Irena Hajnsek is with the Institute of Environmental Engineering, Swiss Federal Institute of Technology, 8093 Zürich, Switzerland, and also with the Microwaves and Radar Institute, German Aerospace Center, 82234 Wessling, Germany (e-mail: irena.hajnsek@dlr.de).

SAR interferometer developed by the German Aerospace Center (DLR) [19] and is providing high resolution coregistered single-look complex data. Thanks to its single-pass nature with a temporal baseline on the order of milliseconds to seconds, the retrieval of sea ice topography becomes possible despite the dynamic nature of sea ice [20].

TanDEM-X InSAR data have been used to retrieve the sea ice topography in numerous studies. Dierking *et al.* [21] examined the potential of deriving sea ice topography from several single-pass spaceborne InSAR configurations and assessed the influence of different factors on measurement accuracy such as sea ice motion, penetration depth, and snow layer. From TanDEM-X InSAR data, Dammann *et al.* [11] retrieved the height of ridges in the landfast ice near Utqiavik, confirming the capability of InSAR to estimate the topography of ridges. Focusing on snow-free multiyear ice, the sea ice topographic height derived from TanDEM-X data by InSAR processing shows good agreement with the measurements from laser profiler and photogrammetry [22]. Recently, Marbouti *et al.* [23] assessed the formation and movement of ridges in the landfast sea ice using TanDEM-X InSAR data. Until now, the majority of the published sea ice topographic studies have been based on the InSAR technique, which is an effective tool for height estimation.

However, there are two major problems with regards to the InSAR technique: the penetration bias depending on the electromagnetic wavelengths and the height sensitivity that increases with longer baselines. First, the InSAR digital elevation model (DEM) is actually a measurement of the radar phase scattering center height. The height bias induced by electromagnetic waves penetration into snow and ice leads to inaccuracy of an InSAR DEM, especially for the low-salinity sea ice with snow cover. For sensors operating at *X*-band, the penetration depth of sea ice ranges from ~ 0.05 to ~ 1 m, depending on the sea ice type, salinity, and temperature [24]. The snow layer yields a greater range of the penetration depth depending on the water content. Dry snow has a penetration depth up to hundreds of wavelengths [25]. Second, for the thin ice with its height of tens-of-centimeters, it is challenging to accurately retrieve the heights in the same order due to the limitation of the baseline configuration in the northern and southern hemisphere [21]. Therefore, to generate an accurate topographic map for various types of sea ice, additional pieces of information are needed to combine with the InSAR technique.

SAR polarimetry provides information on the scattering processes and is a useful tool to characterize sea ice properties. Comprehensive explanations of physical properties in sea ice relevant to electromagnetic scattering mechanisms are given in [24] and [26]. These studies inferred different scattering mechanisms from different types of sea ice and provided a theoretical basis for sea ice observation from polarimetric SAR (PolSAR) imagery. Nghiem *et al.* [27], [28] proposed a composite model, establishing a link between the observed polarimetric signatures to the measured sea ice properties. The polarimetric signatures are also used for sea ice classification [11], [29], [30] and ice thickness estimation [31], [32]. Dammann *et al.* [11] linked an *L*-band polarimetric classification to specific roughness regimes,

which is important to assess ice trafficability. Nevertheless, how the polarimetric signature responds to the variation of sea ice topography is not fully understood. In this study, we attempt to bridge the gap between the polarimetric signature and sea ice topography and to answer whether the polarimetric signature can be a proxy of sea ice topography.

The combination of polarimetric and interferometric techniques through polarimetric SAR Interferometry (Pol-InSAR) [33] can characterize the vertical structure across different scattering mechanisms and is capable of estimating the penetration depth. Some applications of Pol-InSAR include monitoring of glacier and land ice [34]–[36]. However, to our knowledge, no previous work has investigated the feasibility of sea ice topographic retrieval by Pol-InSAR via a suitable scattering model. The sensitivity of Pol-InSAR signatures to the properties of sea ice also needs further study.

In this article, we investigate the polarimetric behavior for the derivation of sea ice topography from dual-polarimetric single-pass InSAR data. The data are collected from coordinated TanDEM-X and airborne-based measurements, covering the western Weddell Sea, Antarctica. The SAR images contain several types of ice, including: new ice, thin ice, thick ice, and deformed ice with ridges, detailed in Table I. This article studies the relation between the polarimetric signatures and sea ice topography. Three polarimetric signatures: copolar coherence γ_{coPol}, copolar phase ϕ_{coPol}, and maximum polarization-dependent phase difference $\Delta\phi_{\text{maxPol}}$ are extracted and analyzed for various sea ice types and topographic heights. A new sea ice topographic map is generated by merging polarimetric signature γ_{coPol} into InSAR processing to compensate the penetration bias. Thereby a sea ice height retrieval comparable to optical DEMs, which measures freeboard including the snow layer, is achieved. A positive correlation between ϕ_{coPol} and the topographic height suggests that ϕ_{coPol} can be a proxy of thin sea ice topographic characterization. For thick and deformed ice with ridges, the observation suggests that the oriented volume scattering should be assumed when employing the Pol-InSAR technique for height inversion. All these investigations are validated against coordinated airborne measurements [37]. The study of polarimetric behavior for the derivation of sea ice DEM in this article lays the foundation for future modeling of sea ice topography and sea ice subsurface structure characterization from polarimetric single-pass InSAR data.

The organization of this article is as follows. The study area and datasets are introduced in Section II. Section III presents the processing of datasets. Experimental results and discussions are elaborated in Section IV and Section V, respectively. Finally, the conclusion is drawn in Section VI.

II. DATASETS AND TEST SITE

On October 29, 2017, a coordinated campaign between the NASAs Operation IceBridge (OIB) airborne mission and the DLR's TanDEM-X satellite mission, named as OIB/TanDEM-X Coordinated Science Campaign (OTASC), offered a unique opportunity to measure sea ice topography in Antarctica [37].

TABLE I
TYPES OF ICE ACCORDING TO THE TOPOGRAPHIC HEIGHT AND MORPHOLOGY FROM DMS

Ice types (see Fig. 3 for details)	Description	Topographic height including snow cover (m)
New ice	Contains frazil ice, grease ice, pancake ice, and small floes (diameter $20 - 100$ m) Snow free	tens of centimeters
Thin ice	Locates near to the leads Rough/smooth surface Has snow cover	about $0 - 0.8$ m
Thick ice	Contains large floes (diameter 100 m $- 4$ km) Smooth surface Has snow cover	about $0.8 - 1.6$ m
Deformed ice	Contains large floes Rough surface Undergoes ridging process Has snow cover	about $1.6 - 3$ m

Based on the OTASC data, Dammann *et al.* [38] proved the potential for InSAR to map the topography of icebergs.

A. Digital Mapping System (DMS)

The DMS is one of the OIB airborne instruments, which is acquiring a set of different data. This study uses two products from the DMS sensor: the DMS airborne digital camera images [39] and the DMS airborne digital elevation models [13]. The details of the two products are given as follows.

The DMS airborne digital camera captures natural color and panchromatic imagery, named as DMS images. The DMS images are geolocated and orthorectified in GeoTIFF format. The spatial resolution ranges from 0.015 to 2.5 m depending on the flight altitude [39]. The DMS images used in this study were acquired at UTC 22:30 Oct. 29, 2017, with a spatial coverage of around 5.8 by 8.8 km.

The DMS DEM is generated by photogrammetric techniques and is adjusted with calibrated LIDAR altimetry measurements. It measures the sea ice elevation including the snow cover. The DMS DEM has a spatial resolution of ~ 40 by ~ 40 cm. The data are acquired on a 16 km transect with a swath width of 400 m [13]. The acquisition took place at around UTC 17:45 Oct. 29, 2017. The data format is provided in GeoTIFF with a Polar Stereographic South map projection and is referenced to WGS-84 ellipsoid. There is about 6-h temporal gap between the DMS DEM and TanDEM-X satellite acquisitions.

B. Tandem-X

The German TanDEM-X mission is a single-pass SAR interferometer that is collecting two images with nearly no temporal gap. The two images acquired from slightly different viewing angles over the same footprint can be used to generate a digital elevation model of the earth surface [19]. The system is operating in *X*-band at a wavelength of 3 cm. For the studied area, the data collection took place at UTC 23:41 October 29, 2017, in

a bistatic mode. The InSAR pair is a Coregistered Single look Slant range Complex (CoSSC) product with dual-polarization (HH and VV) in StripMap mode. The incidence angle of the scene center is 34.8°. The resolution and the pixel spacing are 1.2×6.6 m and 0.9×2.7 m in slant range and azimuth, respectively. The effective perpendicular baseline $b_\perp$ is 175.9 m and the along-track baseline b_{al} is 201.9 m. The height of ambiguity is 32.4 m.

C. Test Site

The test site is located in the western Weddell Sea, which is close to the east coast of the Antarctic Peninsula. It is about 10 km east of the Jason Peninsula and about 20 km away from Larsen-C ice shelf. From the Polar Pathfinder dataset [40], the daily sea ice motion vectors of the test site on October 29, 2017, are primarily towards southeastern direction with an average value of $\sim 2.57 \pm 0.32$ cm/s [40], shown in Fig. 1. Note that the sea ice motion vectors are derived from several specific sensors (see [40] for details) with a 1-day temporal resolution and a 25 km-grid spatial resolution. The average value means an average of the sea ice motion vectors from the same particular day.

An overview of the test site location is given in Fig. 2(a) (left) and a zoom-in in Fig. 2(a) (right). The studied SAR image and the adjacent scene, which is acquired one second afterwards are presented in Fig. 2(a) (right) to give an overall illustration of the sea ice area. Here, the studied TanDEM-X intensity image (green part) overlaid by the DMS flight track covers a 50×20 km sea ice region. Another zoom in is shown in Fig. 2(b), where the DMS images and the DMS DEM tracks are superimposed on the SAR intensity image. From the DMS images, the sea ice structure is visible and can be used to characterize sea ice types. A smaller part (red area), denoted as the region of interest (ROI), contains large floes whose diameters range from 100 m to maximum 4 km. The diameter values are manually measured from the DMS image. In order to specify the ice types in the
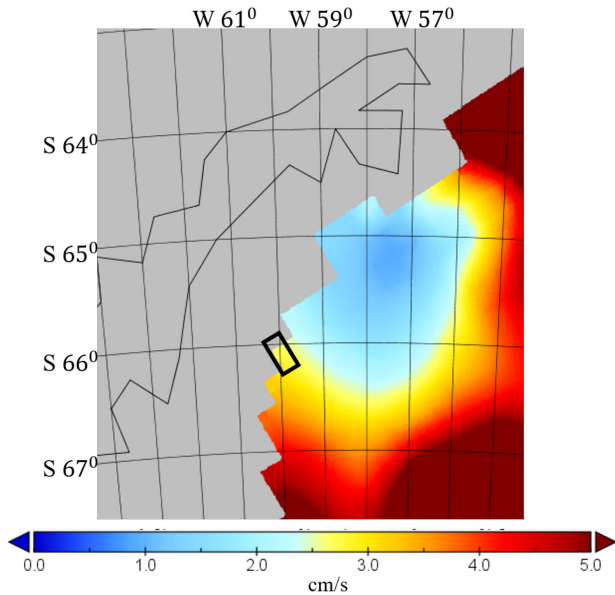
Fig. 1. Daily sea ice motion vectors on October 29, 2017. The black rectangle shows the location of the test site.

sea ice undergoes a significant amount of deformation resulting in ridges and large variations of topographic heights.

III. DATA PROCESSING

A. DMS DEM

The postprocessing of the DMS DEM contains four main steps: reprojection, mosaic, geocoding, and calibration. First, the DMS DEMs are reprojected from Polar Stereographic to WGS84 geographic grid. Since each file has a 400 m by 400 m spatial coverage, the second step is the mosaic of adjacent files into a large portion, which is a 16 km transect with a swath width of 400 m. Third, the merged DMS DEM is geocoded into the SAR coordinate system and resampled into the same resolution as the SAR image with the GAMMA software. Finally, the DMS DEMs are calibrated to the local sea level by selecting the water surface reference from DMS images.

B. Data Coregistration

Due to the 6-h temporal gap between the acquisitions of DMS DEM and TanDEM-X SAR, data coregistration is employed to cancel the shift and thus ensure an effective pixel-by-pixel comparison. The cross-correlation method together with a manual adjustment is used to achieve an accurate data coregistration in radar coordinates. In the studied image, the outside of the ROI is covered with new ice, and the ROI is mainly thick and deformed ice surrounded by thin ice, shown in Fig. 5. The strong dynamics and the fewer strong backscattering features in the new-ice area lead to severe misregistration between the two datasets. For the new-ice area, the smoother ice surface without snow coverage gives relatively low backscattering intensity than the thicker and rougher ice in the ROI. The amount of strong backscattering features (e.g., deformed ice structures and rough snow surface) are significantly reduced in the new-ice area. Therefore, it is challenging to select the distinguishable ice features to calculate the shift distance and direction effectively. More sophisticated coregistration methods are needed to achieve a precise estimation of the shift [42], which is beyond the scope of this article. Hence, only the ROI covered by thick and deformed ice is coregistered and used for quantitative comparison in the following experiments. The 16 km transect [yellow line in Fig. 2(b)] overlaid by the DMS flight track within the ROI is divided into several segments. Each segment contains 11×100 pixels in range and azimuth corresponding to about 1 km length (note that the pixel spacing is about 10×10 m in range and azimuth after the SAR multilook processing in Section III-C). At the center of each segment, the normalized cross-correlation between 2-D gray-scaled DMS DEM image (11×100 pixels in range and azimuth) and SAR intensity image (11×100 pixels in range and azimuth) is applied to each segment, respectively. Coregistration is done according to the shifts in azimuth and range direction calculated from the normalized cross correlation. Manual adjustment is performed based on the normalized cross-correlation result to obtain an optimal colocation of the two datasets. Note that the maximum shift among all segments is 60 m along the range direction. Eight well-coregistered segments

ROI, the DMS image of Area-A labeled in Fig. 2(b) is enlarged in Fig. 3(a). According to the surface morphology observed from DMS images and the height from DMS DEMs, three types of ice are defined: thin ice, thick ice, and deformed ice. The thin ice mainly exits near to the leads, with height ranging from $0 - 0.8$ m. As labeled in Fig. 3(a), the thin ice with a smooth surface has a lower topographic height than the one with a rough surface. The ice presenting a smooth surface with height values from 0.8 to 1.6 m is defined as thick ice. When thick ice undergoes ridging and rafting process, the surface becomes rough and the height arises significantly. This type of ice is defined as deformed ice whose height is above 1.6 m and up to 3 m. Note that these three types of ice all have snow cover, and the height given here refers to the ice elevation including the snow-depth above the local sea level. The sea ice outside the ROI is defined as new ice. Fig. 3(b) reveals the details over Area-B [labeled in Fig. 2(b)]. The new-ice area is mainly covered by frazil ice and grease ice. Due to the rough water condition in Antarctica, pancake ice and rafting with height up to 0.4 m are observed. Small-floes with diameters from 20 to 100 m also occur. From the DMS images, the ice surface outside the ROI is snow-free for most parts. The four ice types above are summarized in Table I and will be referred in the following sections.

A comparison between the test site (see Fig. 2) and the schematic representation (see Fig. 4) [41] further clarifies the ice types that occur in the test site. The sea ice attached to land is fast ice, which can be observed from the adjacent SAR image in Fig. 2(a). Further away from the coastline, the sea ice consists of small floes with diameter ranging from 20 to 100 m (sketched in Fig. 4 and observed in Fig. 2(b)). The small-floe ice is new-formed and drifted with the wind and the currents. The large floes with diameter $100 - 4$ km (denoted in Fig. 4) corresponds to the thick and deformed ice within the ROI Fig. 2(b). In this region, the
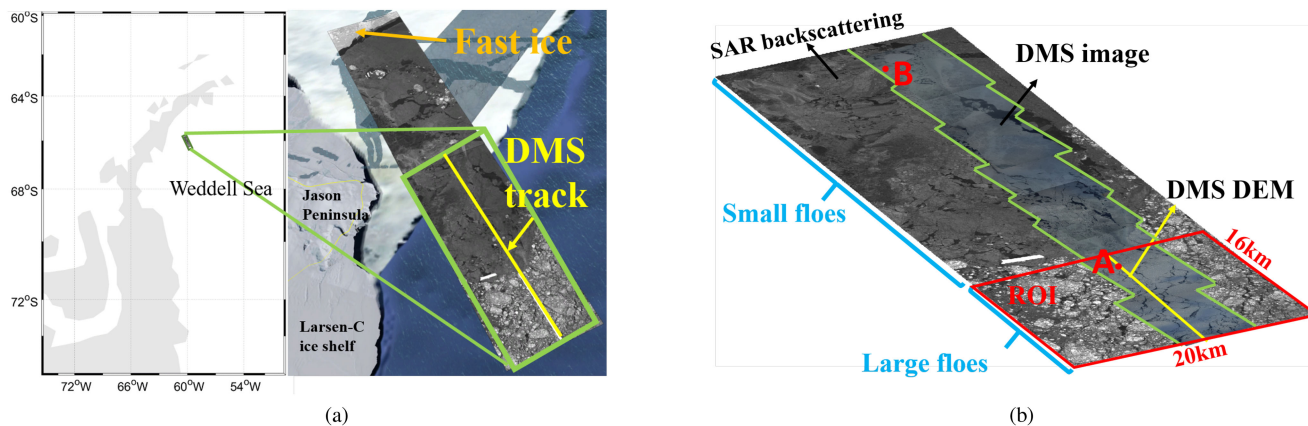
Fig. 2. (a) Geo-location of the test site. The green rectangle indicates the studied SAR backscattering intensity image. The yellow line indicates the DMS flight track. (b) Merge of the SAR backscattering intensity image (HH polarization) and the DMS airborne digital camera images. The red rectangle indicates the region of interest (ROI). The yellow line indicates the overlapping DMS DEM data. The green lines delineate the boundaries of the DMS images (optical).
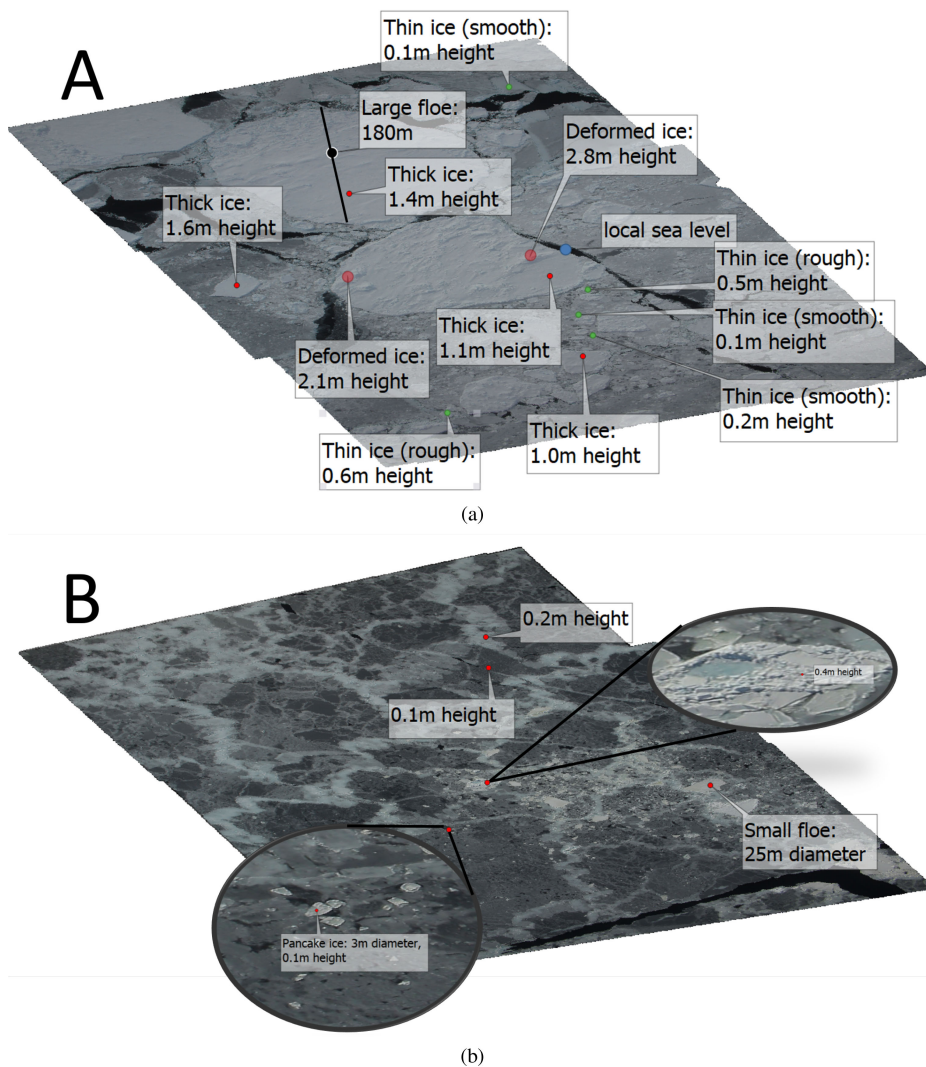

Fig. 3. Illustration of sea ice types from the DMS images (optical) of Area A and B in Fig. 2(b). The height refers to the sea ice elevation (including snow) above local sea level measured by the DMS DEMs. (a) Zoom-in of Area A. (b) Zoom-in of Area B.
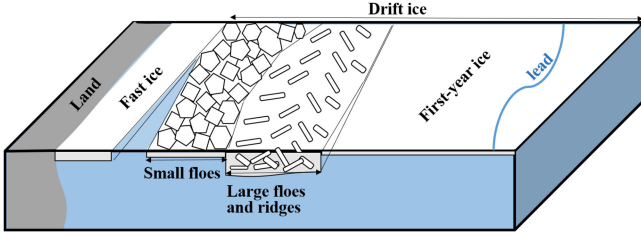
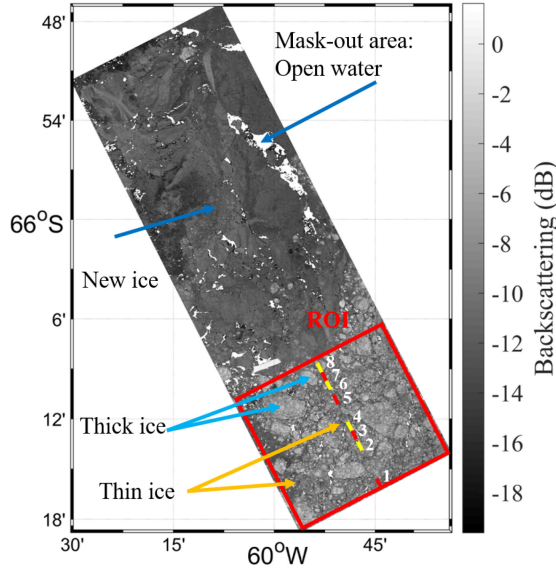Fig. 4.   Schematic of sea ice zonation in the Weddell Sea.

Fig. 5.   SAR backscattering intensity image in HH polarization including 8 experimental segments along the DMS flight track.

denoted in Fig. 5 are selected for quantitative analyses based on the following two principles. First, the height standard deviation σ_h of each segment should be below 0.5 m [21]. Second, there should exist distinct ice features, which can be used to visually check the coregistration result.

C. InSAR

The InSAR pair considered in this article is generated as the CoSSC products; thus, the coregistration and common spectral band filtering in range and azimuth have already been processed [43]. The remaining InSAR processing includes interferogram generation, flat earth removal, interferogram filtering, low-coherence area mask, phase unwrapping, and phase-to-height conversion. All the abovementioned steps are carried out with the GAMMA software.

In single-pass interferometry, the SAR instrument acquires two observations s_1 and s_2 with a temporal lag on the order of milliseconds. The complex interferogram γ and interferometric phase ϕ_γ can be generated as [25]

$$\gamma = s_1 s_2^* \tag{1}$$

$$\phi_\gamma = \arg\{s_1 s_2^*\} \tag{2}$$

where symbol $(^*)$ denotes the complex conjugate.

For scatterers lying in a plane $\Delta z = 0$, the phase gradient can be related to the effective perpendicular baseline $b_\perp$. It is called the flat-earth component of the interferometric phase, a high-frequency component of the phase signal, which can be removed by the process of flat-earth removal using the GAMMA software. Then, an adaptive filter [44] is applied to the flat-earth removed interferogram.

The interferometric coherence is a measurement of signal correlation between two acquisitions. It can be calculated by [25]

$$\tilde{\gamma}_{\text{InSAR}} = \frac{< s_1 s_2^* >}{\sqrt{< s_1 s_1^* >< s_2 s_2^* >}} \tag{3}$$

where the symbol $< . >$ denotes an ensemble average. Here, a 4×12 window in azimuth and slant range is applied to estimate $\tilde{\gamma}_{\text{InSAR}}$. The magnitude of the interferometric coherence $|\tilde{\gamma}_{\text{InSAR}}|$ is derived for both HH and VV polarizations separately and has been then averaged [shown in Fig. 6(a)]. However, the coherence differences between HH and VV are marginal. $|\tilde{\gamma}_{\text{InSAR}}|$ less than 0.3 is masked out and will not be considered in the following processing.

From the interferometric coherence, the phase variance $\sigma_{\phi_\gamma}^2$ can be estimated by the Cramer–Rao bound [45]

$$\sigma_{\phi_\gamma}^2 = \frac{1}{2N} \frac{1 - \gamma_{\text{InSAR}}^2}{\gamma_{\text{InSAR}}^2} \tag{4}$$

where N is the number of looks used to produce the multilook interferogram and the interferometric coherence. The phase variance is used to quantify the uncertainty of the InSAR-derived height. The uncertainty is calculated as a standard deviation of the height σ_h [25]

$$\sigma_h = \frac{h_a}{2\pi} \sigma_{\phi_\gamma} \tag{5}$$

where h_a is the height of ambiguity. From (4) and (5), it can be observed that the choice of number of looks N determines the height standard deviation σ_h, which is suggested to be less than 0.5 m to guarantee a reliable sea ice height retrieval [21]. In order to make sure that the average σ_h is below 0.5 m, a 4×12 window in azimuth and slant range is applied to our processing, corresponding to a $\sim 10 \times 10$ m spatial size. The σ_h for the whole image is calculated based on the average value of $|\tilde{\gamma}_{\text{InSAR}}|$ from HH and VV polarizations, shown in Fig. 6(b).

In the case of sea ice topographic height retrieval, the measured interferometric phase ϕ_γ is defined by [21]

$$\phi_\gamma = \phi_{\text{topo}} + \phi_{\text{mov}} + \phi_{\text{bias}} + 2\pi n, n = 0, \pm 1, \pm 2 \dots \tag{6}$$

where ϕ_{topo} denotes the phase resulting from the height variation of the ground surface, ϕ_{mov} denotes the phase contributed by the sea ice movement (drift), and ϕ_{bias} denotes the phase caused by surface and volume scattering effects. In the process of interferogram generation, no drift-induced phase is found visually. Quantitatively, ϕ_{mov} for a baseline b_{al} in along-track interferometry is [25]

$$\phi_{\text{mov}} = -\frac{2\pi u_{\text{LOS}} b_{\text{al}}}{v\lambda} \tag{7}$$

where u_{LOS} is the line-of-sight velocity, $v \approx 7$ km/s is the ground velocity of the SAR platform, $b_{\text{al}} = 201.9$ m is the
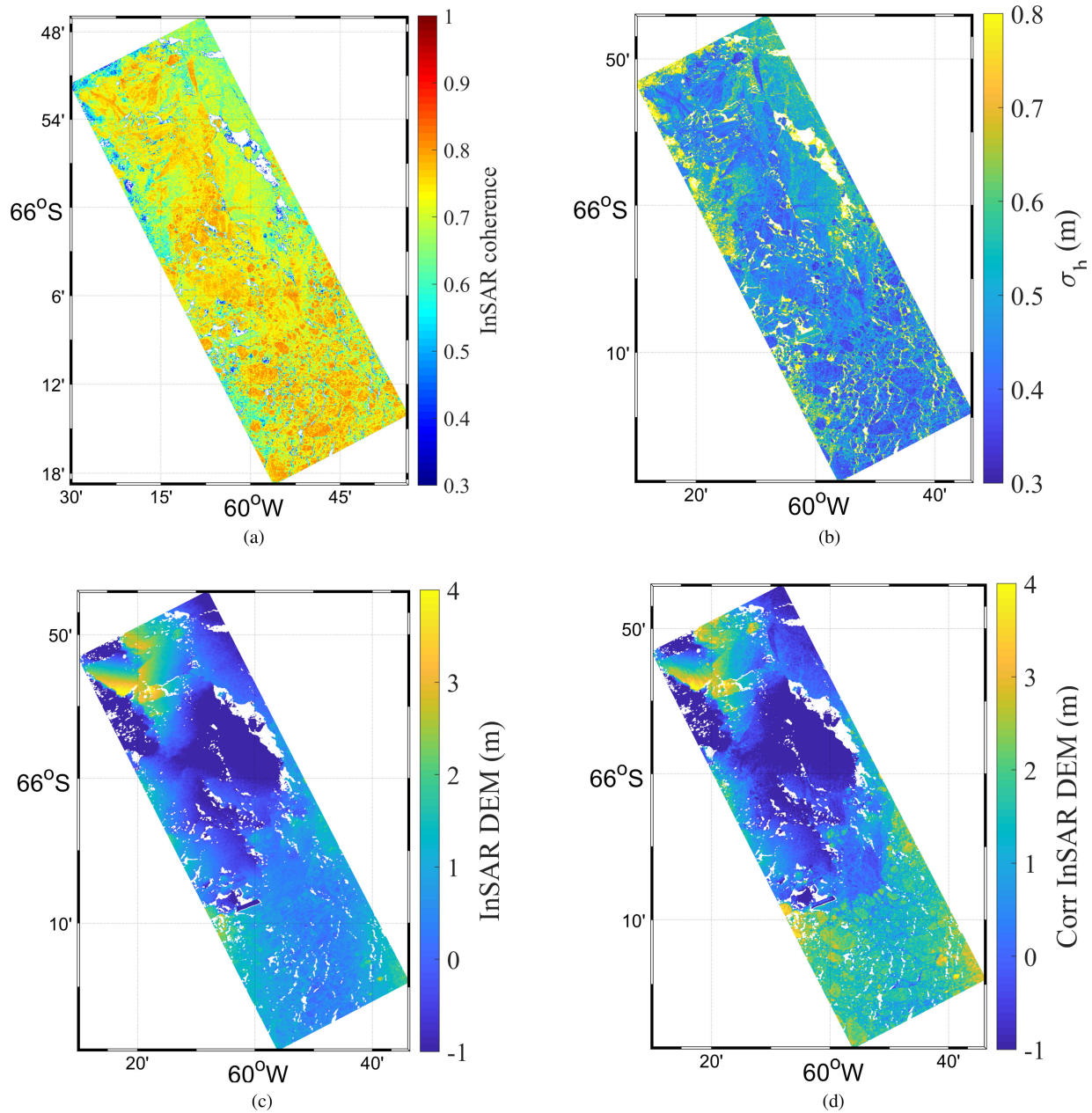
Fig. 6. InSAR products. (a) Interferometric coherence (average of HH and VV polarizations). (b) Height standard deviation σ_h (average of HH and VV polarizations). (c) Original InSAR DEM (average of HH and VV polarizations). (d) CorrInSAR DEM based on the proposed method.

along-track baseline, and $\lambda = 0.031$ m is the radar wavelength as in TanDEM-X. As discussed in Section III-B, we assume that the 60 m across-track shift results from ice drift during the 6-h temporal gap, thus corresponding to $u = 0.003$ m/s. With $u_{\text{LOS}} = u \sin \theta$, where the incidence angle of the scene center θ is 34.8°, $\phi_{\text{mov}} = 0.009$ rad is derived from (7). The corresponding height amounts to $\frac{\phi_{\text{mov}}}{2\pi} h_a = 0.05$ m. Considering that 0.05 m is less than the acceptable height error of 0.5 m [21], the effect of sea ice movement is neglected. It can be expected that no rotation of the ice floe appears during the time of acquisition as no azimuth fringe pattern is observed [46]. Hence, the data processing could be performed directly on the data without further corrections using the GAMMA software and applying

the phase unwrapping followed by the phase-to-height conversion [25], [47]. The InSAR DEM is derived for both HH and VV polarization separately and then averaged [shown in Fig. 6(c)] to avoid potential system noise. However, the height differences between HH and VV are marginal.

D. Polarimetric Signature Extraction

The polarimetric signature of sea ice depends on the material and structural properties as well as the environmental conditions, and surface effects [27]. The material property is inherently subject to material compositions such as pure ice, brine inclusions, and air. Mixing of these constituents gives the

effective permittivity, which characterizes the electromagnetic properties of sea ice [27]. The sea ice structure affects the polarimetric signature in terms of wave propagation, attenuation, and scattering [27]. Environmental conditions such as temperature and salinity are determining factors to derive polarimetric scattering coefficient [27]. Surface effects including roughness, snow, slush, and brine cover further complicate the polarimetric signature of sea ice [27]. All these items are contributing to a composite relation to the polarimetric signature and are crucial to sea ice characterization. This study investigates two polarimetric signatures, the copolar (coPol) coherence γ_{coPol} and coPol phase ϕ_{coPol} [48]

$$\tilde{\gamma}_{\text{coPol}} = \gamma_{\text{coPol}} \cdot e^{i\phi_{\text{coPol}}} = \frac{<s_{\text{VV}}s_{\text{HH}}^*>}{\sqrt{<s_{\text{VV}}s_{\text{VV}}^*><s_{\text{HH}}s_{\text{HH}}^*>}} \quad (8)$$

where s_{HH} and s_{VV} are single look complex images in HH and VV polarization, respectively. The symbol $<.>$ denotes an ensemble average. A 4×12 window in azimuth and slant range is applied to estimate $\tilde{\gamma}_{\text{coPol}}$. In the following, γ_{coPol} and ϕ_{coPol} are calculated on a master and a slave image separately and are averaged to avoid the contribution of potential system noise. However, the differences between the master and slave images are marginal.

E. Pol-InSAR Coherence Region

Snow-covered sea ice is a multilayer media, where the electromagnetic waves can be scattered at the different interfaces. Pol-InSAR gives the location information of the scattering center, and with this knowledge the penetration depth can be inverted. The penetration depth is derived from the maximization of interferometric coherences at different polarizations in the complex plane, which is characterized by the boundaries surrounding the individual complex coherences. The complex interferometric coherence at a given polarization indicated by the unitary vector $\vec{\omega}$ is defined by [25]

$$\tilde{\gamma}(\vec{\omega}) = \frac{<s_1(\vec{\omega})s_2^*(\vec{\omega})>}{\sqrt{<s_1(\vec{\omega})s_1^*(\vec{\omega})><s_2(\vec{\omega})s_2^*(\vec{\omega})>}}. \quad (9)$$

Physically, the extrema of the coherence loci represent the maximum separated phase center in the medium.

For dual polarization, the complex coherences for all possible polarizations $\vec{\omega}$ form an elliptical coherence region in the complex plane. The method to extract coherence region was first developed by Flynn et al. [49] and Tabb et al. [50]. The shape of the elliptical coherence region can be derived analytically [49]. In this study, we calculate the outer boundary of the coherence region following the algorithm in [49] from the dual-polarimetric data. Fig. 7 presents two typical examples. The green ellipse describes the case of a radial coherence region, which shows no evident phase center difference across different polarizations. It can be interpreted as surface-dominant scattering or random volume scattering. On the contrary, the blue ellipse shows the polarization-dependent interferometric phase difference, suggesting that oriented volume scattering is dominant for the given resolution cell or a multilayered medium should be assumed in the structural modeling. The maximum polarization-dependent
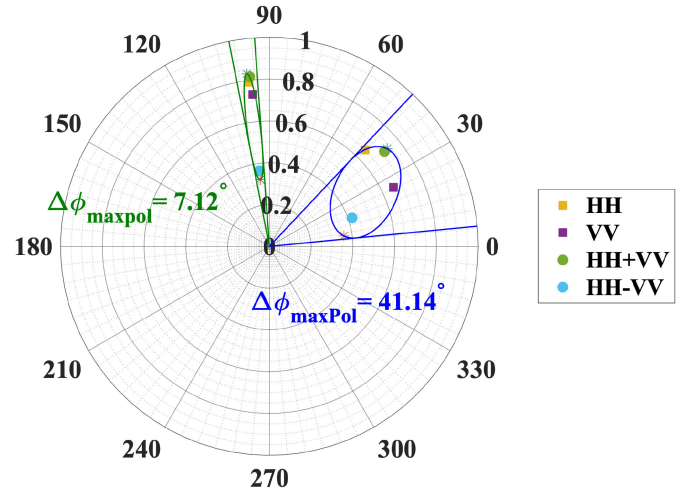

Fig. 7.   Two examples of the Pol-InSAR coherence region in the unit circle.

phase difference (hereafter denoted as maxPol phase $\Delta\phi_{\text{maxPol}}$) is calculated by finding the angle between the two tangent lines (shown in solid lines in Fig. 7) to the ellipse passing through the origin. $\Delta\phi_{\text{maxPol}}$ can be converted to meters via the vertical wavenumber κ_z.

IV. METHODOLOGY AND EXPERIMENTAL RESULTS

In this section, we analyze several polarimetric signatures corresponding to the sea ice topographic height from *X*-band dual-pol InSAR data. Note that the term "sea ice topographic height" throughout the article refers to the sea ice elevation above the local water level including the snow cover.

A. Sea Ice Topographic Height Retrieval

According to (6), the measured interferometric phase ϕ_γ contains the phase bias ϕ_{bias} that could result from the penetration. For thick ice, the electromagnetic waves could penetrate snow and even ice (i.e., low-salinity multiyear ice in Arctic [24]). On the contrary, the DMS DEM measures the sea ice topographic height on the uppermost part, thus inducing a height discrepancy (i.e., penetration bias) between the InSAR-derived height and the optical measurement. In this section, we analyze the penetration bias using the SAR polarimetric diversity and propose a method to correct this bias using the coPol coherence. These corrections allow to obtain a height retrieval comparable to the optical sea ice DEM, which measures freeboard including the depth of snow cover.

Following the InSAR processing described in Section III-C, we generate the sea ice topography of the whole scene, shown in Fig. 6(c). Fig. 8 compares the InSAR-derived topographic height with the DMS DEM for all eight segments. The discrepancy between the TanDEM-X height profile and the DMS height profile is distinct. To quantify this discrepancy, two measurements, the root-mean-square error (RMSE) and the Pearson's r between two profiles, are carried out for each segment. The RMSE is
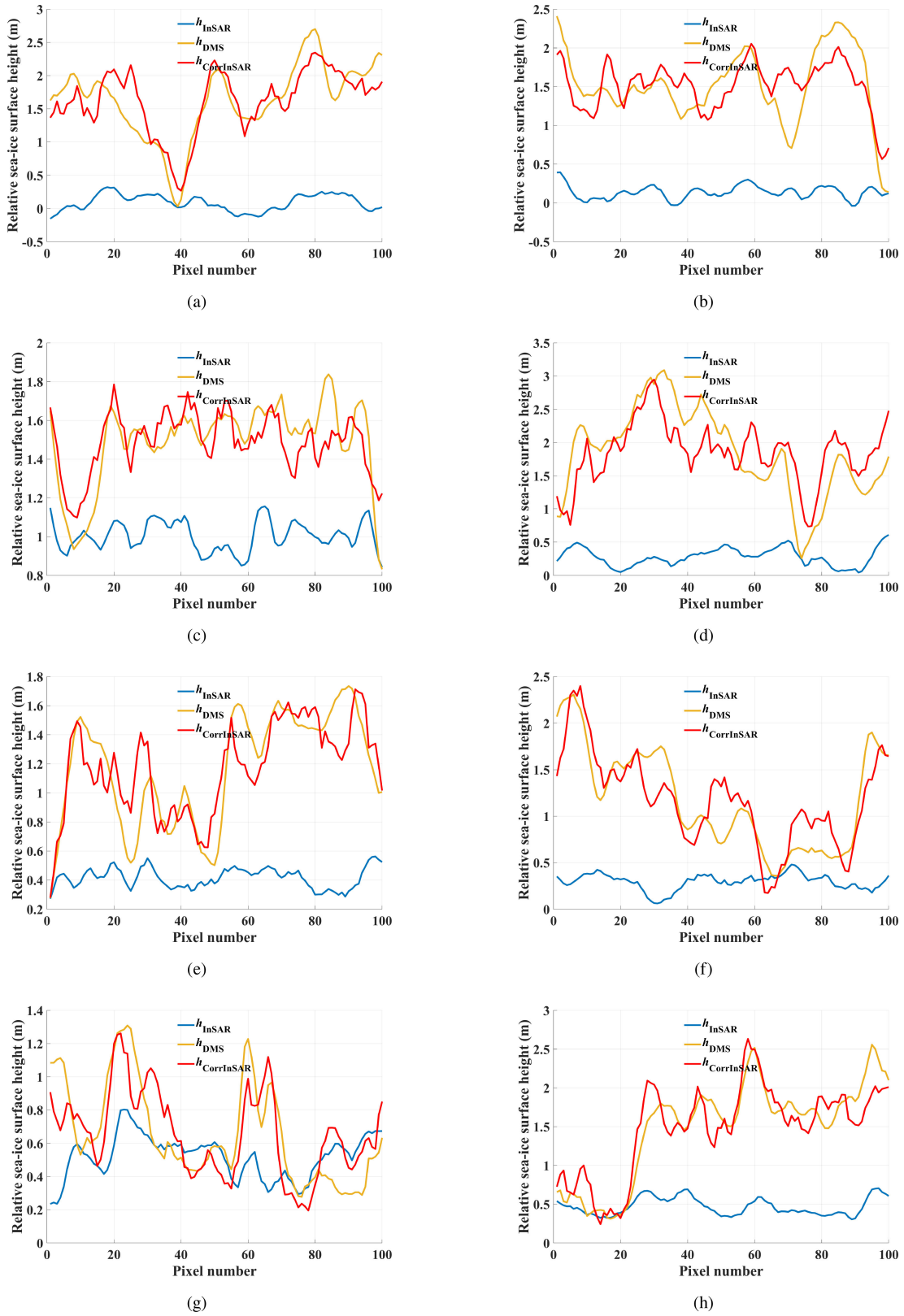
Fig. 8. Sea ice topographic height profiles from TanDEM-X and DMS DEM. Each profile represents the height along a 1×100-pixel section at the center of each segment. (a) Segment 1. (b) Segment 2. (c) Segment 3. (d) Segment 4. (e) Segment 5. (f) Segment 6. (g) Segment 7. (h) Segment 8.

TABLE II
QUANTITATIVE ANALYSES OF THE SEA ICE TOPOGRAPHIC HEIGHT DERIVED
FROM TANDEM-X

Segment	RMSE (m)		r	
	h_{InSAR}	$h_{\text{CorrInSAR}}$	h_{InSAR}	$h_{\text{CorrInSAR}}$
1	1.63	**0.31**	0.11	**0.82**
2	1.45	**0.35**	0.29	**0.67**
3	0.53	**0.15**	0.27	**0.74**
4	1.70	**0.47**	0.01	**0.70**
5	0.85	**0.23**	0.08	**0.80**
6	1.05	**0.30**	−0.35	**0.84**
7	0.34	**0.20**	0.07	**0.74**
8	1.18	**0.26**	0.37	**0.91**

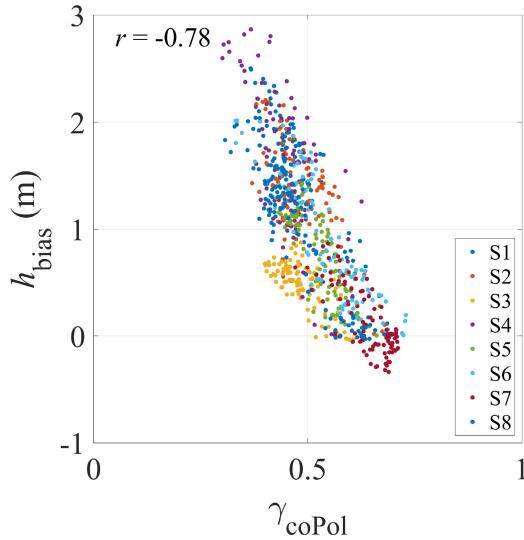Fig. 9. Correlation between the h_{bias} and the γ_{coPol}.

Fig. 10. Correlation between the CorrInSAR DEM and the DMS DEM.

defined as

$$\text{RMSE} = \sqrt{\frac{1}{N} \sum_{N=1}^{N} (h_{\text{InSAR}} - h_{\text{DMS}})^2} \qquad (10)$$

where h_{InSAR} denotes the height derived from TanDEM-X by InSAR processing, h_{DMS} denotes the height measured by DMS, and N is the number of pixels of each transect. For all eight segments, RMSE and r are given in Table II. The mean RMSE is about 1.09 m, and the correlation between InSAR DEM and DMS DEM is not strong. The discrepancy between the InSAR DEM and the DMS DEM could result from the penetration of electromagnetic waves into the snow (see Section V for details). In this case, an appropriate bias-correction method is required to generate an accurate sea ice DEM.

The bias between the DMS DEM h_{DMS} and the InSAR height h_{InSAR} can be calculated as

$$h_{\text{bias}} = h_{\text{DMS}} - h_{\text{InSAR}}. \qquad (11)$$

The γ_{coPol} is calculated according to (8). For each segment, h_{bias} is negatively correlated to γ_{coPol}, shown in Fig. 9 and Table III. The γ_{coPol} varies from 0.8 to 0.2 corresponding to a topographic height variation of 0 to 3 m.
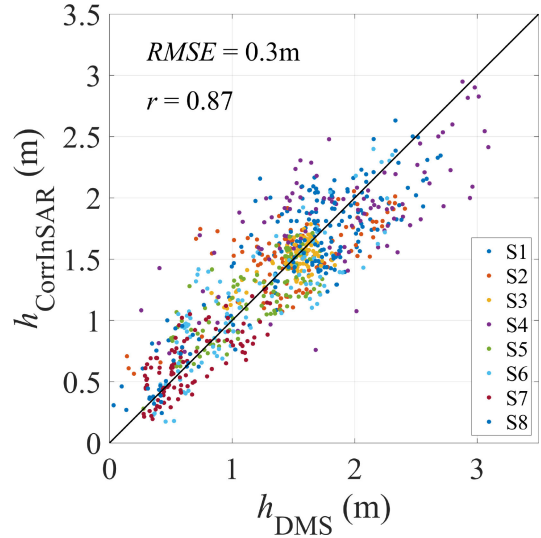
Based on the abovementioned observation, γ_{coPol} is used to correct the InSAR DEM. A linear function is defined as

$$\hat{h}_{\text{bias}} = k \cdot \gamma_{\text{coPol}} + b \qquad (12)$$

where $\hat{h}_{\text{bias}}$ is the height bias derived from the function, k and b are estimated by the least-squares method for each segment. For all eight segments, the mean and standard deviation of k and b are -5.34 ± 1.33 and 3.66 ± 0.90, respectively. The corrected InSAR (CorrInSAR) surface height $h_{\text{corr InSAR}}$ is calculated as

$$h_{\text{corr InSAR}} = h_{\text{InSAR}} + \hat{h}_{\text{bias}}. \qquad (13)$$

The $h_{\text{corr InSAR}}$ for all eight segments are shown in Fig. 8. Visual comparison illustrates that the profiles of $h_{\text{corr InSAR}}$ present much higher agreement with the h_{DMS} than those of h_{InSAR}. Quantitatively, from Table II, the $h_{\text{corr InSAR}}$ has much lower RMSE and higher r than the original InSAR height (i.e., h_{InSAR}). Fig. 10 compares the $h_{\text{corr InSAR}}$ and h_{DMS} for all eight segments. The RMSE and r for all segments are 0.29 m and 0.87, respectively, indicating the effectiveness of applying γ_{coPol} to correct sea ice topographic height. A more accurate sea ice DEM can be generated by merging the polarimetric signature into InSAR processing. In the case without DMS DEM, the $\hat{h}_{\text{bias}}$ can be estimated with the mean value of $k = -5.34$ and $b = 3.66$. The CorrDEM of the whole image is illustrated in Fig. 6(d).

B. Analyses of Polarimetric Signatures

This section analyzes the polarimetric signatures in terms of various sea ice types and topographic heights. According to (8), the coPol coherence γ_{coPol} and coPol phase ϕ_{coPol} are calculated and illustrated in Fig. 11.

1) Polarimetric Signatures Related to Ice Type: In Fig. 11(a), the new-ice region shows the highest γ_{coPol}, with $\gamma_{\text{coPol}} > 0.65$ approximately, followed by the thin-ice region, with $0.5 < \gamma_{\text{coPol}} \leq 0.65$. The γ_{coPol} of the thick-ice region is lower than 0.5. From Fig. 11(b), the ϕ_{coPol} presents the highest value ranging from about $10°$ to $40°$ in the thick-ice region. For the thin-ice
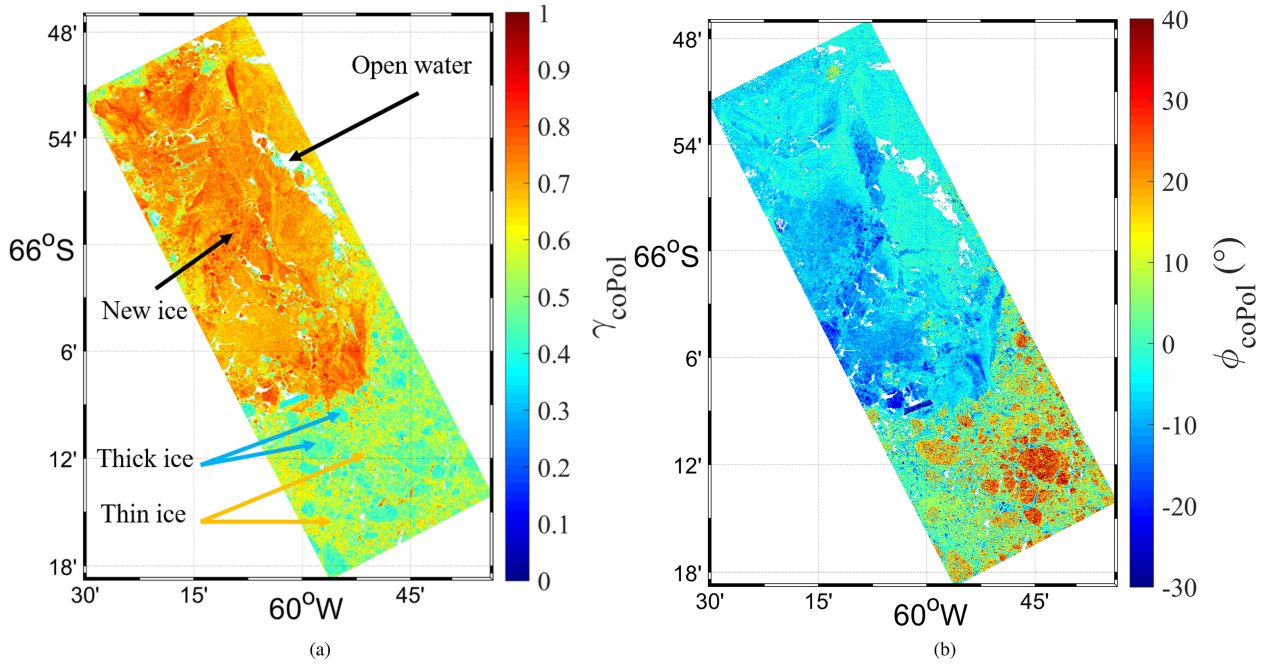
Fig. 11. PolSAR products. (a) coPol coherence γ_{coPol}. (b) coPol phase ϕ_{coPol}.

region, the ϕ_{coPol} ranges from $5°$ to $10°$. The ϕ_{coPol} distributes from negative value to $5°$ in the new-ice region.

Explanations involve different scattering mechanisms depending on various inclusions and structures in various types of ice. The surface layers such as snow, slush, and brine cover also account for the result.

The thin ice, especially the new ice, includes a high concentration of brine inclusions [51], [52], and, thus, the penetration of the X-band electromagnetic waves into the thin and new ice is marginal. In this case, the surface scattering is dominant. For new ice, the γ_{coPol} is high due to the snow-free smooth surface where almost no electromagnetic waves depolarization and copolarimetric decorrelation occur [25]. The ϕ_{coPol} is around $0°$ [53], [54] when the surface is covered by homogeneous, isotropic, and transparent medium. If the medium has an anisotropic structure, such as the ellipsoidal brine inclusions, the signal delay becomes polarization dependent, and the ϕ_{coPol} deviates from $0°$. The ellipsoidal brine inclusions in the new ice are preferentially oriented in vertical direction [27], leading to a positive anisotropy and, thus, a slightly negative ϕ_{coPol} value [55]. For thin ice with a thin snow cover, the snow-air interface can increase the surface roughness [56], [57] and is displayed with a relatively lower γ_{coPol} than the new ice. The negative anisotropy and positive ϕ_{coPol} value are predicted based on the horizontally elongated oblate particles contained in the fresh snow layer [55], [58]. A model based on the birefringent property can explain the observed ϕ_{coPol} in this case [58].

Thick and deformed ice presents larger small-scale surface roughness due to the superimposed ice at the snow-ice interface formed by refrozen snow meltwater [41] and larger large-scale surface roughness because of the ridging and rafting processes [57]. Volume scattering from the snow layer would further intensify the copolarimetric decorrelation (see Section V

for details). Therefore, ϕ_{coPol} significantly deviates from $0°$ and γ_{coPol} value is greatly reduced. If the medium is highly inhomogeneous, the depth of the scattering center becomes polarization dependent, resulting in different scatterers for each polarization [58]. In this case, γ_{coPol} is below 0.5 [58], and Pol-InSAR method is needed to measure the polarization-dependent scattering centers [33].

2) Polarimetric Signatures Related to Surface Height: We further investigate the relation between ϕ_{coPol} and sea ice topographic height at X-band. The segment 1, 2, and 4 are selected for the overall range $(0 - 3\,\text{m})$ of surface heights. The scatter plots are shown in Fig. 12(a)–(c) and the mean ϕ_{coPol} is calculated at the interval of $0.3\,\text{m}$ sea ice topographic height, presented in Fig. 12(d)–(f). An empirical function is employed to fit the samples, which is defined as

$$\hat{\phi}_{\text{coPol}} = a \cdot (1 - \exp{(b \cdot h_{\text{DMS}})}) + c \qquad (14)$$

where $\hat{\phi}_{\text{coPol}}$ is the coPol phase estimated from the above function, a, b, and c are coefficients estimated from observations by the least-squares method. From Fig. 12, we observed that ϕ_{coPol} increases with sea ice topographic height and then becomes saturated. Besides, ϕ_{coPol} becomes more scattered (higher standard deviation) with increasing sea ice topographic height.

For the sea ice topographic height below $1\,\text{m}$, the ϕ_{coPol} is positively correlated to the sea ice topographic height. The anisotropic structure resulting from the ellipsoidal brine inclusions in ice and the oblate particles in the fresh snow, leads to the polarization-dependent signal delay and, in turn, increases the phase difference between copolarization. The continuous feature suggests that ϕ_{coPol} can be an effective proxy for characterizing thin sea ice topography. However, the challenge is that although the trend is clear, every curve has its own shape and gradient. Since the trend is not unique, in order to perform this correction
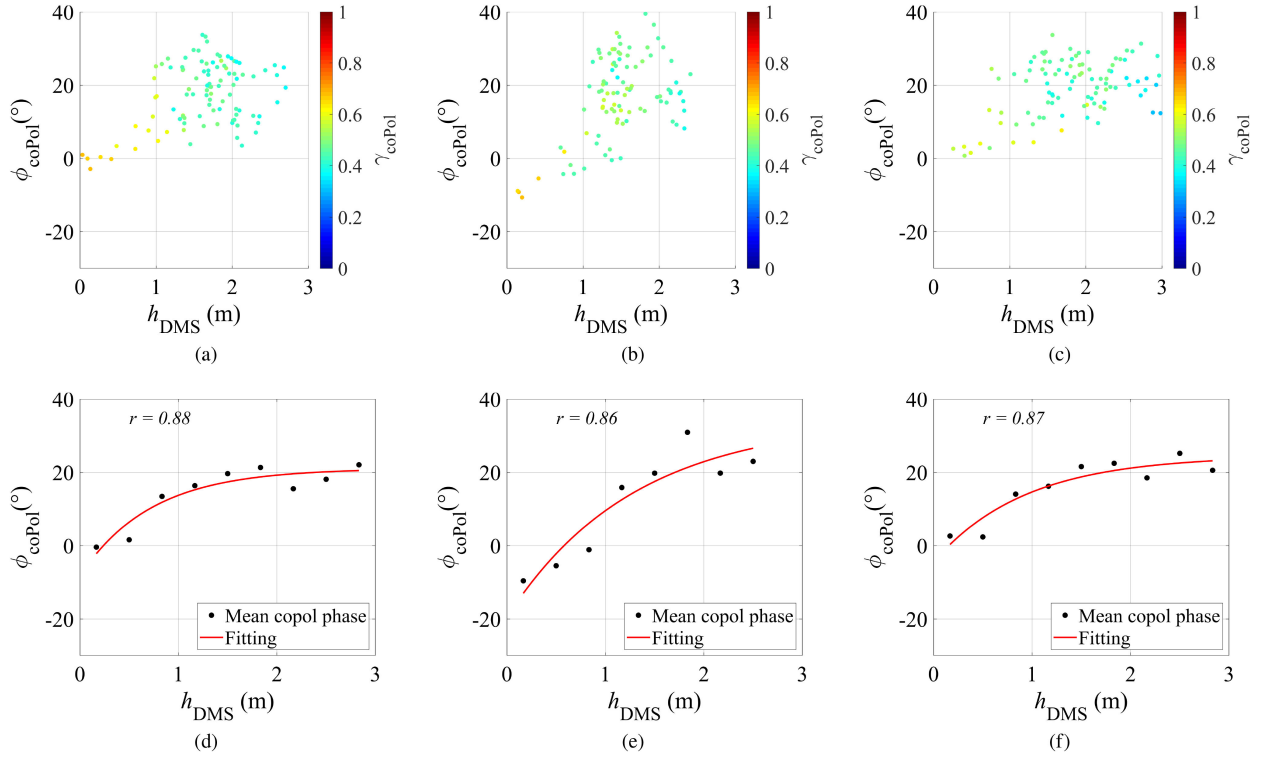
Fig. 12. Relationship between the ϕ_{coPol} and the sea ice topographic height measured by DMS. (a)–(c) ϕ_{coPol} of Segment 1, Segment 2, and Segment 4. (d)–(f) Mean coPol phase and data fitting of Segment 1, Segment 2, and Segment 4.

without prior information, a powerful physical model could be developed and used.

For the sea ice topographic height above 1 m, the ϕ_{coPol} becomes scattered and weakly correlated to the sea ice topographic height. In the studied area, the height above 1 m (including snow depth) corresponds to the thick and deformed ice with ridges, as illustrated in Table I and Fig. 3(a). In this case, the depth of the scattering center becomes polarization dependent, resulting in different scatterers for each polarization [58]. These different scatterers determine the phase of the signal. However, the coherent sum of all scatterers within one resolution cell would lead to a description of the polarimetric scattering centers without a phase location in height. Using the combination of polarimetry and interferometry, the polarization-dependent scattering centers in height can be estimated [33]. The following section further investigates the Pol-InSAR observables.

C. Analyses of Pol-InSAR Coherence Region

The maxPol phase $\Delta\phi_{\text{maxPol}}$ is calculated according to Section III-E and converted to the depth of different phase center d_{maxPol} in meters via the vertical wavenumber κ_z, shown in Fig. 13. Note that when the coherence region encircles the origin, tangent line to the ellipse passing through the origin does not exist, and thereby the $\Delta\phi_{\text{maxPol}}$ are not be performed.

The new-ice region in general shows a radial shape of phase centers across polarizations. The values of $\Delta\phi_{\text{maxPol}}$ and d_{maxPol} are around zero. The $\Delta\phi_{\text{maxPol}}$ is noisy due to the low backscattering power of new ice. Coherence at low power is sensitive to disturbances such as radar system noise and calibration

errors [49]. The radial Pol-InSAR coherence region is typical for the new-ice region, indicating that surface scattering is dominant. On the contrary, the $\Delta\phi_{\text{maxPol}}$ in the ROI ranges from $-15°$ to $-5°$. It reveals that the spread shape of the coherence region is dominant for the snow-covered thick and deformed ice. The spread phase centers among different polarizations forms an ellipsoid coherence region and can be interpreted as oriented volume scattering. The preferential oriented volume for thick and deformed ice induces polarization-dependent phase center. In order to estimate the topography of snow-covered thick ice, different scattering distribution functions for each polarization set is needed to develop an inversion model using Pol-InSAR.

V. DISCUSSION

The sea ice properties in Arctic and Antarctic sea ice are significantly different due to the diverse growth conditions [59], [60]. In the following, we discuss the differences of ice salinity and snow-cover properties between the Antarctic and Arctic, respectively. These two sea ice characteristics are relevant to radar penetration and topographic height retrieval.

Gow *et al.* [51], [52] found the pack ice in Antarctica to be more saline than the Arctic sea ice of comparable age and thickness. Specifically, the mean salinity of 61 first-year ice profiles in Antarctica show values of 4.6‰ [52] compared to 3‰ in the Arctic [61]. The measurements from 14 multiyear profiles in Antarctica indicate an average salinity of 3.5‰ [61], whereas the value in the Arctic is $2 - 2.5$ ‰. Microwaves dielectric behavior of sea ice depends on the ice type, salinity, and temperature [62]. Higher salinity would result in a higher
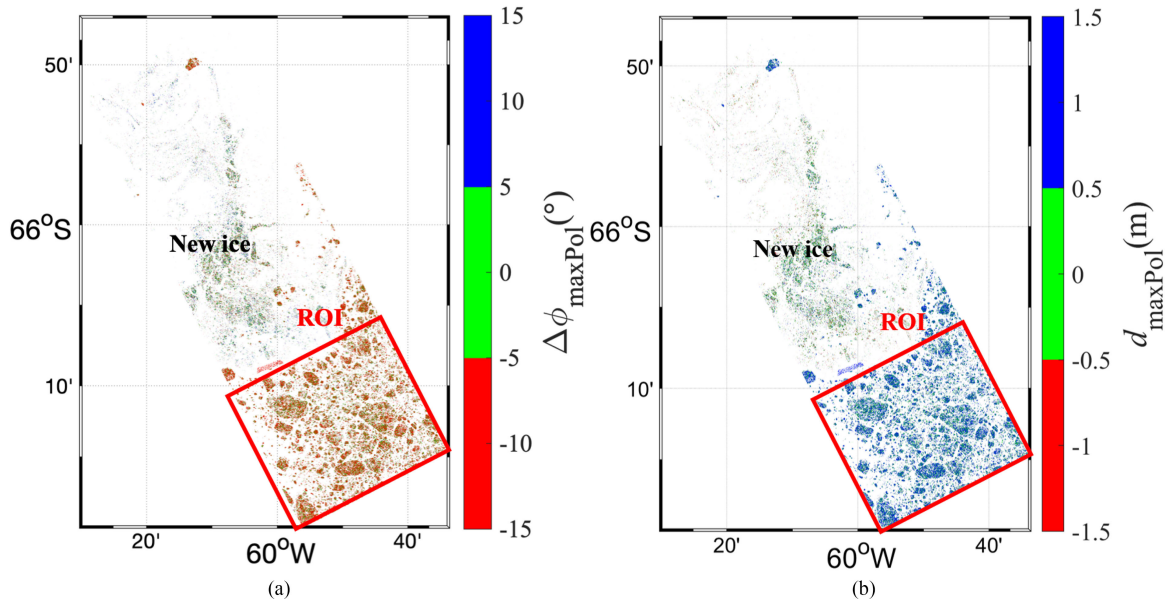
Fig. 13.   Pol-InSAR products. (a) MaxPol phase $\Delta\phi_{\text{maxPol}}$. (b) Depth of different scattering center d_{maxPol}.

extinction coefficient and, thus, a lower penetration depth of electromagnetic waves. At $10\,\text{GHz}$, the penetration depth for $4.4 - 4.6\text{‰}$ salinity sea ice varies from about 0.05 to $0.3\,\text{m}$ at different temperatures [63].

Snow makes a significant contribution to Antarctic sea ice growth and is reported to be thicker as well as wetter than in the Arctic [56], [64], [65]. In the Weddell Sea, the snow thickness on pack ice is measured to be $0.01 - 1.29\,\text{m}$ [56]. Besides, the snow on Antarctic sea ice comprises heterogeneous layers resulted from highly variable temperature and is typically saline when the heavy snow cover on top of the sea ice is getting flooded by the ocean water (i.e., snow flooding) [56]. Electromagnetically, the snow layer affects the microwaves characteristics by its heterogeneity in types, density, salinity, and wetness. The grain-size and water content of snow are two major factors, which determine the penetration of electromagnetic waves [24]. Dry snow yields a penetration depth up to hundreds of wavelength [25]. For wet snow, the penetration depth lies in a range of $0.01 - 0.4\,\text{m}$ with water content from 12% to $<1\%$ [24]. At Ku-band ($10 - 16\,\text{GHz}$), the experiments of Antarctic snow-covered sea ice indicate that the dominant scattering surface of radar could be the snow/ice interface, air/snow interface, or a subsurface layer in between, depending on the snow wetness and density [65]. The mean penetration is around 50% of the mean measured snow depth [65].

Considering the high-salinity ice as well as the thicker and wetter snow in Antarctica, we assume the *X*-band radar can only penetrate into the snow layer rather than the ice. The penetration depth depends on the specific water content, grain size, the salinity of the snow pack, and the temperature. Therefore, the dominant scattering surface of radar would locate at somewhere between the air/snow and snow/ice interface. It results in the height discrepancy between the InSAR DEM and the optical DEM.

The observed inverse relation between γ_{coPol} and topographic height is associated with the surface scattering from several

interfaces and the volume scattering of the snow layer. γ_{coPol} is an indicator of copolarimetric decorrelation, which is sensitive to both small- and large-scale surface roughness variations [66]. The small-scale roughness concerns the ice and snow surface ranging from millimeters to meters. Thicker sea ice presents larger small-scale surface roughness due to the superimposed ice at the snow-ice interface formed by refrozen snow meltwater [41], [56]. Besides, thicker ice presents larger large-scale surface roughness because of the ridging and rafting processes [26]. Although the ridging in Antarctica is less intense than in the Arctic, evidence of ridging occurrence was given in [67]–[69]. Furthermore, the coPol decorrelation is intensified by volume scattering. As the electromagnetic waves propagate into the snow layer, volume scattering occurs when the layer contains enough inhomogeneities (e.g., large-size ice grains, ice lenses, and vertical refrozen structures) [58]. For thick and deformed ice, the stronger (rough) surface scattering together with the volume scattering increase the copolarimetric decorrelation and reduces the γ_{coPol} value.

This study offers a first understanding of the elevation difference between the InSAR DEM and the optical DEM from the OTASC campaign over the Antarctic sea ice. In Section IV-A, following (11)–(13), a new method is developed to achieve a sea ice height retrieval (i.e., $h_{\text{CorrInSAR}}$), which is comparable to the optical DEM (i.e., h_{DMS}). The contribution of this article lies in the identification of the elevation differences and the demonstration of the add-on of polarimetric SAR for sea ice structure estimation. Nevertheless, some limitations of this method need further discussion. First, the h_{DMS} is used to fit the bias function (12) for each segment, and this function is used to derive the $h_{\text{CorrInSAR}}$ for that segment and is compared with the h_{DMS}. Admittedly, this method requires the prior knowledge (i.e., h_{DMS}) to fit (12), and thereby is not an automatically stand-alone method, which can be directly applied to sea ice topographic retrieval. However, the effectiveness of this method indicates that the SAR polarimetry

TABLE III
CORRELATION BETWEEN THE h_{BIAS} AND THE γ_{COPOL}

Segment	1	2	3	4	5	6	7	8
r	−0.82	−0.64	−0.71	−0.72	−0.80	−0.86	−0.76	−0.89

carries significant topographic information and has the potential to characterize sea ice topography. This method provides a link between the elevation difference and the SAR polarimetry and is an essential step forward toward the development of a comprehensive algorithm for sea ice topographic retrieval. To further interpret the bias function (12) and achieve an automatic sea ice topography algorithm more ancillary data, such as the specific snow depth and temperature, are required. These data would be available in OTASC Level-4 products in the future, offering us an opportunity to give a comprehensive interpretation of the bias function. Second, the validation is performed on thick and deformed ice, and therefore, the results are directly applicable to this typology of ice. However, to extend this to other types of ice, we need more extensive validation campaigns with satellite and airborne images taken simultaneously. Third, due to the limited coregistered data, we could not assess the transferability of these results on other data sets. As future work, we will investigate the use of a larger dataset and explore the potential to extrapolate the method to other test sites.

It is of interests to mention the potential occurrence of icebergs in the sea ice region. Icebergs are pieces of freshwater ice that have broken away from a glacier or an ice shelf and are floating in the ocean [70]. Icebergs and sea ice own different characteristics and properties [71], and it is important to achieve a separation of these two. From SAR images, icebergs are expected to have higher backscattering intensity due to their rougher surface than sea ice [38], [72]. Hence, several methods are developed for iceberg detection assuming a distinct contrast between icebergs and background (seawater and sea ice) [73]–[75]. However, snow on the top of sea ice and the occurrence of deformed ice can decrease the contrast between the icebergs and sea ice [76]. In order to successfully distinguish icebergs from sea ice in this case, some advanced algorithms are proposed based on C-band polarimetric SAR techniques [77]–[79]. In this study, the objective is characterizing sea ice. The classification of icebergs and sea ice is beyond the scope of this article. Using the DMS optical images acquired over the test site, we confirmed it is the sea ice rather than icebergs that are covering the studied region.

This study only investigates copolarimetric signatures since the SAR images are acquired in HH and VV polarization. Nowadays, with the increasing availability of quad-pol and dual-pol (i.e., HH/VV and HV/VH) acquisitions over polar regions, information from cross-pol images would be advantageous to estimate the sea ice topography. First, an accurate sea ice classification can be achieved with multipolarization (including HV/VH) SAR images based on the backscattering coefficient [80], [81] and the polarimetric signatures [11], [82]. The reliability of the sea ice estimated height error depends on the ratios between sea ice thickness, penetration depth, and height of ambiguity of a specific volume, which varies with ice types [21]. Therefore, the spatial distribution of various types of ice provides valuable prior knowledge for sea ice topographic mapping. Second, cross-pol

signatures such as the cross-pol ratio (the ratio of backscattering power between HV/VH and HH/VV polarization) can be an indicator of the degree of polarization [25], which is related to the sea ice topography and roughness [32]. The theoretical model predicts that the cross-pol ratio is positively correlated to the sea ice roughness [32]. Therefore, it would be interesting to investigate the potential of retrieving topographic height using cross-pol signatures and compare them with the result using the copolar signatures. Furthermore, the cross-pol images together with copolar images can be used to estimate the penetration depth and locate the top surface (sea ice/snow surface) by Pol-InSAR techniques [33].

VI. CONCLUSION

This article investigates the X-band SAR polarimetric behavior for the derivation of sea ice topography. The data were acquired from TanDEM-X SAR and OIB DMS over the western Weddell Sea, Antarctica. The studied SAR image contains new ice, thin ice, thick ice, and deformed ice with ridges. The area (ROI) overlaid by the DMS DEM data is used for a quantitative comparison. For the area covered by the thick and deformed ice, the penetration bias is negatively related to γ_{coPol}. In order to compensate for the penetration bias, a new method is proposed by merging the polarimetric signature γ_{coPol} into the single-pass interferometric processing. The newly generated DEM has an improved RMSE value of 0.3 m compared to an RMSE of 1.09 m of the original DEM. We also calculated γ_{coPol}, ϕ_{coPol}, and $\Delta\phi_{\mathrm{maxPol}}$ for various sea ice types and topographic heights. For the thin ice, γ_{coPol} is higher than 0.5 and ϕ_{coPol} is positively correlated to the sea ice topographic height, suggesting that ϕ_{coPol} can be an effective polarimetric parameter for thin sea ice topographic characterization. For the thick and deformed ice with ridges, γ_{coPol} is below 0.5 due to the strong surface and volume decorrelation. The phase between HH and VV polarization becomes independent. Therefore, the ϕ_{coPol} is scattered and shows no relation with sea ice topographic height, indicating the necessity of investigating the Pol-InSAR signature $\Delta\phi_{\mathrm{maxPol}}$ for the thick ice. Larger $\Delta\phi_{\mathrm{maxPol}}$ of the thick ice reveals the spread shape of coherence region, which can be interpreted as the oriented volume scattering. It reveals that the sea ice may have different vertical structure functions in each polarization. Therefore, the Pol-InSAR method with oriented volume scattering model is necessary for measuring the scattering centers in thick and deformed ice.

This study indicates the dual-polarimetric single-pass InSAR data are promising to be exploited in the future for a wide-scale reconstruction of sea ice topography (i.e., freeboard including the snow layer). Further work includes developing advanced algorithms for sea ice topographic retrieval from PolSAR and Pol-InSAR techniques. With more ancillary measurements (e.g., snow depth and ice freeboard height) available in the future, we

will take an in-depth look into the comprehensive scattering mechanisms for Antarctic snow-covered sea ice.

REFERENCES

[1] W. F. Weeks and S. F. Ackley, "The growth, structure, and properties of sea ice," in *The Geophysics of Sea Ice.* New York, NY, USA: Springer, 1986, pp. 9–164.

[2] P. Rampal, J. Weiss, and D. Marsan, "Positive trend in the mean speed and deformation rate of Arctic sea ice, 1979–2007," *J. Geophysical Res.*, Oceans, vol. 114, no. C5, pp. C05013.1–C05013.14, 2009.

[3] D. N. Thomas and G. S. Dieckmann, *Sea Ice: An Introduction to Its Physics, Chemistry, Biology and Geology.* Hoboken, NJ, USA: Wiley, 2008.

[4] T. Garbrecht, C. Lüpkes, J. Hartmann, and M. Wolff, "Atmospheric drag coefficients over sea ice–validation of a parameterisation concept," *Tellus A, Dyn. Meteorol. Oceanogr.*, vol. 54, no. 2, pp. 205–219, 2002.

[5] G. Castellani, C. Lüpkes, S. Hendricks, and R. Gerdes, "Variability of arctic sea-ice topography and its impact on the atmospheric surface drag," *J. Geophysical Res.*, Oceans, vol. 119, no. 10, pp. 6743–6762, 2014.

[6] T. Tin and M. O. Jeffries, "Sea-ice thickness and roughness in the ross Sea, Antarctica," *Ann. Glaciol.*, vol. 33, pp. 187–193, 2001.

[7] K. J. Frost, L. F. Lowry, G. Pendleton, and H. R. Nute, "Factors affecting the observed densities of ringed seals, *Phoca hispida*, in the Alaskan Beaufort sea, 1996–99," *Arctic*, vol. 52, pp. 115–128, 2004.

[8] C. David, F. L. Schaafsma, J. A. van Franeker, B. Lange, A. Brandt, and H. Flores, "Community structure of under-ice fauna in relation to winter sea-ice habitat properties from the Weddell sea," *Polar Biol.*, vol. 40, no. 2, pp. 247–261, 2017.

[9] S. F. Ackley and C. Sullivan, "Physical controls on the development and characteristics of Antarctic sea ice biological communitiesa review and synthesis," *Deep Sea Res. I, Oceanographic Res. Papers*, vol. 41, no. 10, pp. 1583–1604, 1994.

[10] D. O. Dammann, H. Eicken, A. R. Mahoney, F. J. Meyer, and S. Betcher, "Assessing sea ice trafficability in a changing arctic," *Arctic*, vol. 71, no. 1, pp. 59–75, 2018.

[11] D. O. Dammann *et al.*, "Traversing sea icelinking surface roughness and ice trafficability through SAR polarimetry and interferometry," IEEE J. Sel. Topics Appl. Earth Observ. Remote Sens., vol. 11, no. 2, pp. 416–433, Feb. 2018.

[12] D. V. Divine *et al.* , "Photogrammetric retrieval and analysis of small scale sea ice topography during summer melt," *Cold Regions Sci. Technol.*, vol. 129, pp. 77–84, 2016.

[13] R. Dotson and J. Arvesen, *IceBridge DMS L3 Photogrammetric DEM*, version 1, Boulder, CO, USA: NASA, 2012

[14] W. Dierking, "Laser profiling of the ice surface topography during the Winter Weddell Gyre study 1992," *J. Geophysical Res.*, Oceans, vol. 100, no. C3, pp. 4807–4820, 1995.

[15] S. L. Farrell, T. Markus, R. Kwok, and L. Connor, "Laser altimetry sampling strategies over sea ice," *Ann. Glaciol.*, vol. 52, no. 57, pp. 69–76, 2011.

[16] B. E. Schutz, H. J. Zwally, C. A. Shuman, D. Hancock, and J. P. DiMarzio, "Overview of the ICESat mission," *Geophysical Res. Lett.*, vol. 32, no. 21, pp. L21801.1–L21801.4, 2005.

[17] W. Abdalati *et al.*, "The ICESat-2 laser altimetry mission," *Proc. IEEE Proc. IRE*, vol. 98, no. 5, pp. 735–751, May 2010.

[18] P. A. Rosen *et al.*, "Synthetic aperture radar interferometry," *Proc. IEEE Proc. IRE*, vol. 88, no. 3, pp. 333–382, Mar. 2000.

[19] G. Krieger *et al.*, "TanDEM-X: A satellite formation for high-resolution SAR interferometry," *IEEE Trans. Geosci. Remote Sens.*, vol. 45, no. 11, pp. 3317–3341, Nov. 2007.

[20] E. Rodriguez and J. Martin, "Theory and design of interferometric synthetic aperture radars," *IEE Proc. F Radar Signal Process.*, vol. 139, no. 2, pp. 147–159, Apr. 1992.

[21] W. Dierking, O. Lang, and T. Busche, "Sea ice local surface topography from single-pass satellite InSAR measurements: A feasibility study," *Cryosphere*, vol. 11, no. 4, pp. 1967–1985, 2017.

[22] T. G. Yitayew *et al.*, "Validation of sea-ice topographic heights derived from TanDEM-X interferometric SAR data with results from laser profiler and photogrammetry," *IEEE Trans. Geosci. Remote Sens.*, vol. 56, no. 11, pp. 6504–6520, Nov. 2018.

[23] M. Marbouti *et al.*, "Evaluating landfast sea ice ridging near UtqiaġVik Alaska using TanDEM-X interferometry," *Remote Sens.*, vol. 12, no. 8, p. 1247, 2020.

[24] M. Hallikainen and D. P. Winebrenner, "The physical basis for sea ice remote sensing," *Microw. Remote Sens. Sea Ice*, vol. 68, pp. 29–46, 1992.

[25] S. Cloude, *Polarisation: Applications in Remote Sensing.* London, U.K.: Oxford Univ. Press, 2010.

[26] W. Tucker, D. K. Perovich, A. J. Gow, W. F. Weeks, and M. R. Drinkwater, "Physical properties of sea ice relevant to remote sensing," *Microw. Remote Sens. Sea Ice*, vol. 68, pp. 9–28, 1992.

[27] S. Nghiem, R. Kwok, S. Yueh, and M. Drinkwater, "Polarimetric signatures of sea ice: 1. theoretical model," *J. Geophysical Res.*, Oceans, vol. 100, no. C7, pp. 13665–13679, 1995.

[28] S. Nghiem, R. Kwok, S. Yueh, and M. Drinkwater, "Polarimetric signatures of sea ice: 2. experimental observations," *J. Geophysical Res.*,Oceans, vol. 100, no. C7, pp. 13681–13698, 1995.

[29] H. Wakabayashi, T. Matsuoka, K. Nakamura, and F. Nishio, "Polarimetric characteristics of sea ice in the sea of Okhotsk observed by airborne L-band SAR," *IEEE Trans. Geosci. Remote Sens.*, vol. 42, no. 11, pp. 2412–2425, Nov. 2004.

[30] S. Singha, M. Johansson, N. Hughes, S. M. Hvidegaard, and H. Skourup, "Arctic sea ice characterization using spaceborne fully polarimetric L-, C-, and X-band SAR with validation by airborne measurements," *IEEE Trans. Geosci. Remote Sens.*, vol. 56, no. 7, pp. 3715–3734, Jul. 2018.

[31] D. Winebrenner, L. Farmer, and I. Joughin, "On the response of polarimetric synthetic aperture radar signatures at 24-cm wavelength to sea ice thickness in Arctic leads," *Radio Sci.*, vol. 30, no. 2, pp. 373–402, 1995.

[32] J.-W. Kim, D.-j. Kim, and B. J. Hwang, "Characterization of Arctic sea ice thickness using high-resolution spaceborne polarimetric SAR data," *IEEE Trans. Geosci. Remote Sens.*, vol. 50, no. 1, pp. 13–22, Jan. 2012.

[33] K. P. Papathanassiou and S. R. Cloude, "Single-baseline polarimetric SAR interferometry," *IEEE Trans. Geosci. Remote Sens.*, vol. 39, no. 11, pp. 2352–2363, Nov. 2001.

[34] J. J. Sharma, I. Hajnsek, K. P. Papathanassiou, and A. Moreira, "Estimation of glacier ice extinction using long-wavelength airborne Pol-InSAR," *IEEE Trans. Geosci. Remote Sens.*, vol. 51, no. 6, pp. 3715–3732, Jun. 2013.

[35] G. Fischer, G. Parrella, K. Papathanassiou, and I. Hajnsek, "Interpretation of Pol-InSAR signatures from glaciers and ice sheets at different frequencies," in *Proc. 11th Eur. Conf. Synthetic Aperture Radar*, 2016, pp. 1–6.

[36] G. Fischer and I. Hajnsek, "Dual-pol x-band Pol-InSAR time series of a Greenland outlet glacier," in *Proc. POLINSAR*, 2015, vol. 729, pp. 31–36.

[37] S. Nghiem *et al.*, "Remote sensing of antarctic sea ice with coordinated aircraft and satellite data acquisitions," in *Proc. IEEE Int. Geosci. Remote Sens. Symp.,* 2018, pp. 8531–8534.

[38] D. O. Dammann *et al.*, "Iceberg topography and volume classification using TanDEM-X interferometry," *Cryosphere*, vol. 13, no. 7, pp. 1861–1875, 2019.

[39] R. Dominguez, *IceBridge DMS L1B Geolocated and Orthorectified Images*, version 1. Boulder, CO, USA: NASA, 2010

[40] Tschudi, M., W. N. Meier, J. S. Stewart, C. Fowler, and J. Maslanik, *Polar Pathfinder Daily 25 km EASE-Grid Sea Ice Motion Vectors*, version 4. Boulder, CO, USA: NASA, 2019

[41] F. D. Carsey, *Microwave Remote Sensing of Sea Ice*. Washington, DC, USA: American Geophysical Union, 1992.

[42] T. Kræmer, H. Johnsen, and C. Brekke, "Emulating Sentinel-1 doppler radial ice drift measurements using Envisat ASAR data," *IEEE Trans. Geosci. Remote Sens.*, vol. 53, no. 12, pp. 6407–6418, Dec. 2015.

[43] S. Duque, U. Balss, C. Rossi, T. Fritz, and W. Balzer, "TanDEM-X payload ground segment, CoSSC generation and interferometric considerations," *German* Aerosp. *Center, Oberpfaffenhofen, Germany*, vol. 1, pp. 1–31, May 15, 2012.

[44] R. M. Goldstein and C. L. Werner, "Radar interferogram filtering for geophysical applications," *Geophysical Res. Lett.*, vol. 25, no. 21, pp. 4035–4038, 1998.

[45] M. Seymour and I. Cumming, "Maximum likelihood estimation for SAR interferometry," in *Proc. IEEE Int. Geosci. Remote Sens. Symp.*, 1994, vol. 4, pp. 2272–2275.

[46] R. Scheiber, F. De Zan, P. Prats, L. S. Araujo, M. Künemund, and L. Marotti, "Interferometric sea ice mapping with TanDEM-X: First experiments," in *Proc. IEEE Int. Geosci. Remote Sens. Symp.*, 2011, pp. 3594–3597.

[47] S. Leinss, "Depth, anisotropy, and water equivalent of snow estimated by radar interferometry and polarimetry," Ph.D. dissertation, Dept. Civil, Environ. Geomatic Eng., ETH Zurich, Zurich, Switzerland, 2015.

[48] J.-S. Lee and E. Pottier, *Polarimetric Radar Imaging: From Basics to Applications*. Boca Raton, FL, USA: CRC press, 2009.

[49] T. Flynn, M. Tabb, and R. Carande, "Coherence region shape extraction for vegetation parameter estimation in polarimetric SAR interferometry," in *Proc. IEEE Int. Geosci. Remote Sens. Symp.*, 2002, vol. 5, pp. 2596–2598.

[50] M. Tabb, J. Orrey, T. Flynn, and R. Carande, "Phase diversity: A decomposition for vegetation parameter estimation using polarimetric SAR interferometry," in *Proc. Eur. Conf. Synthetic Aperture Radar*, 2002, vol. 2, pp. 721–724.

[51] A. Gow, S. Ackley, W. Weeks, and J. Govoni, "Physical and structural characteristics of antarctic sea ice," *Ann. Glaciol.*, vol. 3, pp. 113–117, 1982.

[52] A. J. Gow *et al.*, "Physical and structural characteristics of weddell sea pack ice," *Ann. Glaciol.*, vol. 3, pp. 113–117, 1987.

[53] F. T. Ulaby, D. Held, M. C. Donson, K. C. McDonald, and T. B. Senior, "Relating polaization phase difference of SAR signals to scene properties," *IEEE Trans. Geosci. Remote Sens.*, vol. GE-25, no. 1, pp. 83–92, Jan. 1987.

[54] A. Freeman and S. L. Durden, "A three-component scattering model for polarimetric SAR data," *IEEE Trans. Geosci. Remote Sens.*, vol. 36, no. 3, pp. 963–973, May 1998.

[55] S. Leinss, H. Löwe, M. Proksch, J. Lemmetyinen, A. Wiesmann, and I. Hajnsek, "Anisotropy of seasonal snow measured by polarimetric phase differences in radar time series," *Cryosphere*, vol. 10, no. 4, pp. 1771–1797, 2016.

[56] R. A. Massom *et al.*, "Snow on Antarctic sea ice," *Rev. Geophys.*, vol. 39, no. 3, pp. 413–445, 2001.

[57] T. Toyota, R. Massom, K. Tateyama, T. Tamura, and A. Fraser, "Properties of snow overlying the sea ice off east antarctica in late winter, 2007," *Deep Sea Res. II, Topical Stud. Oceanogr.*, vol. 58, no. 9/10, pp. 1137–1148, May 2011.

[58] S. Leinss, G. Parrella, and I. Hajnsek, "Snow height determination by polarimetric phase differences in x-band SAR data," *IEEE J. Sel. Topics Appl. Earth Observ. Remote Sens.*, vol. 7, no. 9, pp. 3794–3810, Sep. 2014.

[59] P. Gloersen, W. Campbell, D. Cavalieri, J. Comiso, C. Parkinson, and H. Zwally, "Arctic and Antarctic sea ice, 1978–1987," Nat. Aeronaut.Space Admin., *Washington, DC, USA*, vol. 290, pp. 1–6, 1992.

[60] J. E. Walsh, "A comparison of Arctic and Antarctic climate change, present and future," *Antarctic Sci.*, vol. 21, no. 3, pp. 179–188, 2009.

[61] G. F. Cox and W. F. Weeks, "Salinity variations in sea ice," *J. Glaciol.*, vol. 13, no. 67, pp. 109–120, 1974.

[62] A. Stogryn and G. Desargant, "The dielectric properties of brine in sea ice at microwave frequencies," *IEEE Trans. Antennas Propag.*, vol. 33, no. 5, pp. 523–532, May 1985.

[63] M. Vant, R. Ramseier, and V. Makios, "The complex-dielectric constant of sea ice at frequencies in the range 0.1–40 GHz," *J. Appl. Phys.*, vol. 49, no. 3, pp. 1264–1280, 1978.

[64] M. Jeffries, K. Morris, W. Weeks, and A. Worby, "Seasonal variations in the properties and structural composition of sea ice and snow cover in the Bellingshausen and Amundsen seas, Antarctica," *J. Glaciol.*, vol. 43, no. 143, pp. 138–151, 1997.

[65] R. C. Willatt, K. A. Giles, S. W. Laxon, L. Stone-Drake, and A. P. Worby, "Field investigations of Ku-band radar penetration into snow cover on Antarctic sea ice," *IEEE Trans. Geosci. Remote Sens.*, vol. 48, no. 1, pp. 365–372, Jan. 2010.

[66] D. Kasilingam, D. Schuler, and J.-S. Lee, "The depolarization of radar backscatter from rough surfaces due to surface roughness and slopes," in *Proc. IEEE Int. Geosci. Remote Sens. Symp.*, 2001, vol. 2, pp. 925–927.

[67] W. Weeks, S. Ackley, and J. Govoni, "Sea ice ridging in the ross sea, antarctica, as compared with sites in the Arctic," *J. Geophysical Res.*, Oceans, vol. 94, no. C4, pp. 4984–4988, 1989.

[68] V. Lytle and S. Ackley, "Sea ice ridging in the eastern Weddell sea," *J. Geophysical Res.*, Oceans, vol. 96, no. C10, pp. 18411–18416, 1991.

[69] H. Granberg and M. Leppäranta, "Helicopterborne remote sensing of Antarctic sea ice using a laser profiler, synchronized video and 70 mm camera during FINNARP-89," in *Proc. 10th IAHR Ice Symp.*, 1990, vol. 3, pp. 313–325.

[70] T. Hamley and W. Budd, "Antarctic iceberg distribution and dissolution," *J. Glaciol.*, vol. 32, no. 111, pp. 242–251, 1986.

[71] M. Kristensen, "Iceberg calving and deterioration in Antarctica," *Prog. Phys. Geography*, vol. 7, no. 3, pp. 313–328, 1983.

[72] R. Williams, W. Rees, and N. Young, "A technique for the identification and analysis of icebergs in synthetic aperture radar images of Antarctica," *Int. J. Remote Sens.*, vol. 20, no. 15/16, pp. 3183–3199, 1999.

[73] C. Wesche and W. Dierking, "Iceberg signatures and detection in SAR images in two test regions of the Weddell sea, Antarctica," *J. Glaciol.*, vol. 58, no. 208, pp. 325–339, 2012.

[74] A. Frost, R. Ressel, and S. Lehner, "Automated iceberg detection using high-resolution x-band SAR images," *Can. J. Remote Sens.*, vol. 42, no. 4, pp. 354–366, 2016.

[75] T. A. Silva and G. R. Bigg, "Computer-based identification and tracking of Antarctic icebergs in SAR images," *Remote Sens. Environ.*, vol. 94, no. 3, pp. 287–297, 2005.

[76] V. Akbari and C. Brekke, "Iceberg detection in open and ice-infested waters using C-band polarimetric synthetic aperture radar," *IEEE Trans. Geosci. Remote Sens.*, vol. 56, no. 1, pp. 407–421, Jan. 2018.

[77] W. Dierking and C. Wesche, "C-band radar polarimetryuseful for detection of icebergs in sea ice?" *IEEE Trans. Geosci. Remote Sens.*, vol. 52, no. 1, pp. 25–37, Jan. 2014.

[78] A. Marino, W. Dierking, and C. Wesche, "A depolarization ratio anomaly detector to identify icebergs in sea ice using dual-polarization SAR images," *IEEE Trans. Geosci. Remote Sens.*, vol. 54, no. 9, pp. 5602–5615, Sep. 2016.

[79] J.-W. Kim, D.-j. Kim, S.-H. Kim, and B.-J. Hwang, "Iceberg detection using full-polarimetric RADARSAT-2 SAR data in west Antarctica," in *Proc. 3rd Int. Asia-Pacific Conf. Synthetic Aperture Radar,* 2011, pp. 1–4.

[80] M. Drunkwater, R. Hosseinmostafa, and P. Gogineni, "C-band backscatter measurements of winter sea-ice in the Weddell sea, Antarctica," *Int. J. Remote Sens.*, vol. 16, no. 17, pp. 3365–3389, 1995.

[81] M. Arkett, D. Flett, and R. De Abreu, "C-band multiple polarization SAR for ice monitoring–what can it do for the Canadian ice service," in *Proc. Envisat Symp., Montreux, Switzerland,* Citeseer, 2007, pp. 23–27.

[82] A. M. Johansson, C. Brekke, G. Spreen, and J. A. King, "X-, C-, and L-band SAR signatures of newly formed sea ice in Arctic leads during winter and spring," *Remote Sens. Environ.*, vol. 204, pp. 162–180, 2018.

Lanqing Huang (Student Member, IEEE) received the B.Sc. degree in communication engineering from Xi'an Jiao Tong University, Xi'an, China in 2015. She is currently working toward the Ph.D. degree with the Institute of Electronic Engineering, Shanghai Jiao Tong University, Shanghai, China.

From October 2018 to September 2020, she was a visiting Ph.D student with ETH Zürich, Zürich, Switzerland. Her research interests include synthetic aperture radar (SAR) image interpretation, interferometric and polarimetric SAR data processing, SAR observation of ocean, and the sea-ice characterization from TanDEM-X imagery.

Irena Hajnsek (Fellow, IEEE) received the Diploma degree (Hons.) from the Free University of Berlin, Berlin, Germany, in 1996, and the Dr. degree (Hons.) from the Friedrich Schiller University of Jena, Jena, Germany, in 2001.

Since November 2009, she has been a Professor of Earth Observation with the Swiss Federal Institute of Technology, Zürich Institute of Environmental Engineering, Zrich, Switzerland, and, at the same time, the head of the Polarimetric SAR Interferometry Research Group with the German Aerospace Center Microwaves and Radar Institute, Wessling, Germany. Since 2010, she has been the Science Coordinator of the German satellite mission TanDEM-X and proposed satellite mission Tandem-L. Her main research interests include electromagnetic propagation and scattering theory, radar polarimetry, SAR and interferometric SAR data processing techniques, and environmental parameter modeling and estimation.

Dr. Hajnsek was the Technical Program Co-Chair Chair of the IEEE IGARSS 2012 in Munich, Germany, and IEEE IGARSS 2019 in Yokohama, Japan. Since 2013, she has been a member of the IEEE GRSS AdCom, and since 2016, she has been the Vice-President of the IEEE GRSS Technical Committees.